Hydrothermally synthesized Cd-doped ZnO nanostructures with efficient sunlight-driven photocatalytic and antibacterial activity

Karuna P. Ghoderao[1] · Shweta N. Jamble[1] · Rohidas B. Kale[1]

Abstract

The doping in the metal oxide is key factors that can affect the photocatalytic and antibacterial activity. In present work, Cd-doped ZnO nanostructures have been synthesized by using a facile hydrothermal method. The sunlight induced photocatalytic activity of Cd-doped ZnO nanostructures was evaluated towards the degradation of methylene blue dye. The antibacterial activity of ZnO nanoparticles against *Staphylococcus aureus* was investigated. The XRD patterns exhibit a wurtzite hexagonal crystal structure with crystallite size in the range of 18–23 nm. Field emission scanning electron microscopy revealed the plate-like morphology of undoped ZnO and it transforms into small nanorods and aggregated irregularly shaped nanoparticles with the incorporation of Cd into ZnO. Energy dispersive spectroscopy analysis confirms the presence of cadmium in Cd-doped ZnO sample. The UV–Visible absorption spectra showed a redshift with an increase in Cd dopant concentration in ZnO. The PL spectra show near band edge emission and defect-related visible emission band. The Cd-doped ZnO exhibits excellent photocatalytic degradation of methylene blue dye compared to undoped ZnO within 30 min. The Cd-doped ZnO (4 wt%) shows maximum photocatalytic degradation efficiency of 84% under sunlight irradiation.

1 Introduction

Environmental pollution and energy crisis are two serious threats in our society. Therefore numerous scientists are focused on to explore possible solutions and seeking energy from different sources. Semiconductor photocatalyst is a promising tool for harvesting solar energy and solve the global problem of the energy crisis and environmental pollution. Photocatalytic activity is a very active field of pollution control. In particular, dye degradation of water pollutants is essential for wastewater treatment due to its low cost, high efficiency and production of no other secondary pollutants [1]. Semiconductor photocatalyst attracted more attention in the field of photocatalyst due to their excellent degradation efficiency for various pollutants. Over the past decades, zinc oxide (ZnO) is the most studied and efficient material for photocatalytic application because of their high stability and a low risk to the environment [2–5]. The hexagonal wurtzite ZnO is n-type II–IV semiconductor compound characterized by the wide direct band gap of 3.37 eV with large exciton

binding energy of 60 meV at room temperature [2]. Due to such interesting properties, ZnO can be used in pigments, gas sensors, optical devices, solar cells, and photocatalysis [6–10]. As ZnO is a wide band semiconductor, it absorbs only ultraviolet region of the solar spectrum. To increase its utility in the visible region of the solar spectrum and enhance the photocatalytic activity, ZnO can be modifying by doping with metal ion [11]. In the case of Cd-doped ZnO nanostructures, Cd^{2+} ion capture photogenerated electrons and restrain recombination of electron and hole, therefore the photocatalytic activity of ZnO material is enhanced [12–14].

Yu et al. [15] were successfully synthesized Mg-doped ZnO (MZO) nanoparticles using polyacrylamide polymer method. The MZO catalyst exhibits excellent photodegradation efficiency of 95% for methylene blue (MB) dye within 45 min under solar irradiation. After nine cycles, catalyst still maintains more than 95% degradation efficiency. Dong et al. [16] reported the ZnO nanoparticles synthesized using a simple sol–gel method showed excellent photocatalytic activity towards MB dye under solar light irradiation. They have also reported that the superoxide radicals $^{\cdot}O_2^{-}$ and h^+ were main active intermediate species during the photocatalysis process. Wang et al. [17] elucidate the graphene hybridized Mg-doped ZnO (MZO)

✉ Rohidas B. Kale
  rb_kale@yahoo.co.in

[1] Department of Physics, The Institute of Science, Madam Cama Road, Mumbai 400032, India

shows excellent photocatalytic activity for MB dye and retain good photocatalytic activity after nine cycle runs. The enhancement of photocatalytic activity was due to coverage of graphene on the surface of MZO nanoparticles and Mg doping concentration. Thirugnanam et al. [18] have been reported that photocatalytic reduction efficiency of CdSe QDs and CdSe/GO nanocomposites were approximately 81.90% and 95.5% respectively. The enhancement in photocatalytic reduction efficiency of CdSe/GO nanocomposites was ascertained to high surface area and reduction of recombination rate of electron–hole pair. Hosseinpour-Mashkani et al. [19] studied the photocatalytic activity of neodymium vanadate ($NdVO_4$) nanoparticles and 97% degradation efficiency was observed for methyl orange (MO) dye. Sobhani-Nasab et al. [20] first time reported the photocatalytic performance of $MnWO_4$/$TmVO_4$ ternary nano-hybrids for the degradation of rhodamine B, 2-naphthol, phenol red and eosin Y under visible light irradiation. Maximum degradation efficiency was observed to be 99.2% in case of rhodamine B dye. Sedighi et al. [21] investigated the $Cu(WO_4)$/NiO nanocomposite exhibited higher photodegradation efficiency than $Cu(WO_4)$ nanoparticles for MO dye under UV irradiation. Kooshki et al. [22] reported that the $PbTiO_3$/carbon dots binary nano-hybrids exhibited highest photodegradation efficiency (100%) than $PbTiO_3$ nanoparticles for the rhodamine B dye. Eghbali-Arani et al. [23] studied the photocatalytic activity of $YbVO_4$ and $YbVO_4$/$CuWO_4$ nanocomposites for MB pollutant. $YbVO_4$ shows 65% photodegradation efficiency while $YbVO_4$/$CuWO_4$ nanocomposites show 100% degradation efficiency within 120 min. They have also studied the effect of ultra sonication on photocatalytic activity of $YbVO_4$/$CuWO_4$ nanocomposites. With ultrasonic irradiation, degradation efficiency was observed to be 100%, whereas without ultrasonication 61% efficiency was observed for $YbVO_4$/$CuWO_4$ nanocomposites. Eghbali-Arani et al. [24] also synthesized the $SmVO_4$ nanoparticles in the presence of lactose as a capping agent and studied photocatalytic properties of $SmVO_4$ nanoparticles for MB and MO dye. The maximum degradation efficiency of 96% was observed for MB dye within 160 min.

For controlled applications of ZnO different kinds of impurity, the dopant can be used in ZnO lattice. The important aim of doping is the band gap modification i.e. increases or decrease in bandgap by impurity doping. Cadmium dioxide (CdO) is n-type semiconductor with the direct bandgap of 2.2 eV [25]. Doping of Cd in ZnO resulted in reductions in bandgap [26] which leads to the tuning of luminescence from ultraviolet to visible region. Cd-doped ZnO powders have been synthesized by various methods including sonochemical method [27], sol–gel synthesis [28], hydrothermal method [25, 29] and chemical synthesis method [30]. Among these methods, the hydrothermal method is simple, low cost, biocompatible and environmentally benign nature, high purity and easily controlled parameters [2, 31].

The main aim of this research work is to synthesize Cd-doped ZnO via hydrothermal method. Effect of different concentration of Cd dopant on the structural, optical, morphological and photocatalytic activity of ZnO materials is systematically studied. We have also studied the antibacterial activity of ZnO nanostructures against *Staphylococcus aureus* (*S. aureus*).

2 Experimental section

2.1 Materials

Zinc acetate dihydrate [$Zn(CH_3COO)_2\cdot2H_2O$], cadmium acetate dihydrate [$Cd(CH_3COO)_2\cdot2H_2O$] and sodium hydroxide (NaOH) were purchased from S D Fine Chem. Ltd. Mumbai and used without further purification.

2.2 Sample preparation

In a typical synthesis, 0.05 M of $Zn(CH_3COO)_2\cdot2H_2O$ and different weight percentage (2, 4 and 6%) of $Cd(CH_3COO)_2\cdot2H_2O$ was dissolved in 70 ml of distilled water. A simultaneously appropriate amount of aqueous solution of NaOH was added gradually in the main mixture to maintain the pH of resultant solution 12. The final solution was transferred to Teflon-lined stainless steel autoclave and the autoclave was put in a hot air oven at the temperature of 180 °C for 24 h. The final products were washed with distilled water and dry at 80 °C for 6 h.

2.3 Characterizations

The crystal structure of synthesized powders was determined by using Rigaku, Miniflex-II X-ray diffractometer ($\lambda = 1.5405$Å) with the 2θ range of 20–80°. Surface morphology was studied using field emission scanning electron microscope (FESEM, Zeiss Ultra 55FE-SEM) and transmission electron microscope (FETEM, Technai G2). The elemental analysis was confirmed by using an energy-dispersive X-ray analyzer (EDXA, Oxford Instrument). The chemical valences and composition of the as-synthesized powders were analyzed by X-ray photoelectron spectroscopy (XPS, PHI 5000 Versa probe-II). The optical measurement was carried out by using UV–visible spectrophotometer (PerkinElmer Lambda 750). The room-temperature photoluminescent spectra were recorded on a fluorescence spectrophotometer (PerkinElmer LS 55).

2.4 Photocatalytic activity study

The photocatalytic activity of MB dye was performed under sunlight irradiation. A typical procedure for the photocatalytic activity of MB dye is as follows. 20 mg of prepared ZnO samples were added to 50 ml aqueous solution of MB dye with constant stirring for 30 min in dark to obtain adsorption–desorption equilibrium. After 30 min, the solution was illuminated under sunlight. An aliquot of 5 ml was collected from solution at an equal interval of time and filtered with Whatman filter paper. The photocatalytic degradation process was monitored by UV–visible spectrophotometer. The percentage degradation of MB dye was determined from the following equation,

$$\text{Percentage degradation } (\eta) = \frac{C_0 - C_t}{C_0} \times 100 \tag{1}$$

where C_0 represents the initial concentration of MB dye at time $t = 0$, C_t represents the concentration of MB dye at time $t = t$.

2.5 Antibacterial activity

The inculums *S. aureus* was prepared in sterile saline water. The sterile nutrient agar was placed in the conical flask. The nutrient agar was allowed to cool and *S. aureus* was added into the flask. The antibacterial activity of undoped ZnO and Cd-doped ZnO (4 wt%) was carried out by disc diffusion method. The Whatman filter paper disc (6 mm diameter) containing ZnO and Cd-doped ZnO (4 wt%) samples were placed on the agar surface using sterile forceps and press slightly for complete contact with the medium. Finally, the disc was incubated at 37 °C for 24 h. The inhibition zones were measured and recorded.

3 Result and discussion

3.1 Structural studies

The crystal structure and average crystallite size of undoped ZnO and Cd-doped ZnO (CZO) for different concentration of Cd were estimated by XRD patterns and presented in Fig. 1. The XRD patterns of all ZnO and CZO samples exhibited a typical hexagonal wurtzite crystal structure (JCPDS card no. 36-1451). All samples shows diffraction peaks at 31.96°, 31.54°, 36.39°, 47.75°, 56.69°, 62.99°, 66.54°, 68.16°, 69.33°, 72.71° and 77.06° corresponding to (100), (002),(101), (102), (110), (103), (200), (112), (201), (004), and (202) planes. The average
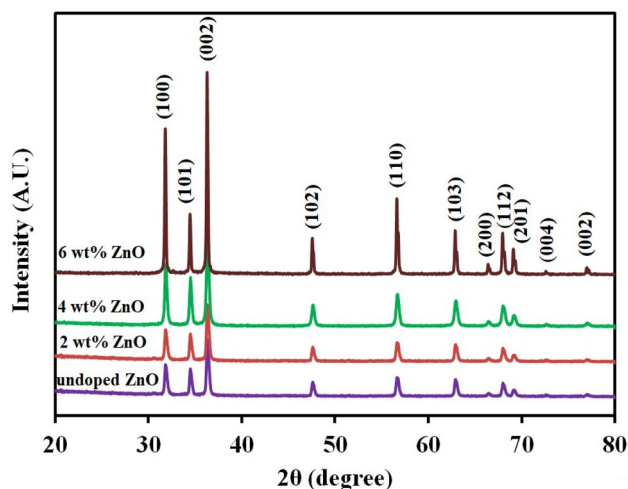

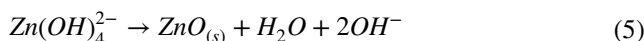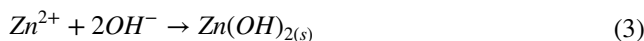**Fig. 1** **a–d** XRD patterns of undoped ZnO and CZO (2, 4 & 6 wt%)

crystallite size of undoped ZnO and CZO was estimated by using Debye-Scherer formula [32],

$$D = \frac{(0.9\lambda)}{(\beta cos\theta)} \tag{2}$$

where D is crystallite size, λ is wavelength of X-ray (1.5406 Å), θ is Bragg diffraction angle and β is full width at half maximum. The average crystallite size was in the range of 18–23 nm.

3.2 Morphological analysis

Figure 2a–d shows FESEM images of undoped ZnO and CZO (2, 4 and 6wt%) materials. As observed from FESEM images ZnO featured a plate-like morphology with different size and shape as shown in Fig. 2a, b. The overall reaction mechanism of ZnO during the hydrothermal method is as follows.

$$Zn^{2+} + 2OH^- \rightarrow Zn(OH)_{2(s)} \tag{3}$$

$$Zn(OH)_2 + 2(OH)^- \rightarrow Zn(OH)_4^{2-} \tag{4}$$

$$Zn(OH)_4^{2-} \rightarrow ZnO_{(s)} + H_2O + 2OH^- \tag{5}$$

The solid white precipitate of zinc hydroxide $Zn(OH)_2$ was formed with the addition of a small amount of NaOH solution to zinc salt solution (Eq. (3)). Further increase in OH^- ions concentration, the earlier formed $Zn(OH)_2$ reacts with excess OH^- and formed stable zinc hydroxide complex growth units $Zn(OH)_4^{2-}$ (Eq. (4)). As the temperature of the resultant solution reached to 180 °C, the preformed $Zn(OH)_4^{2-}$ species decomposes to form tiny ZnO nuclei (Eq. (5)). The crystal growth of ZnO was significantly
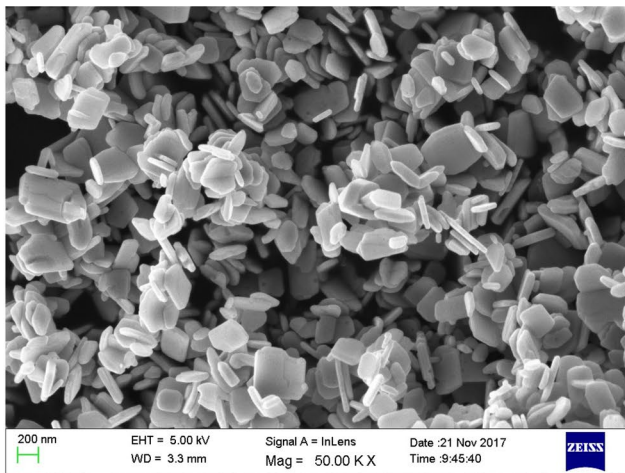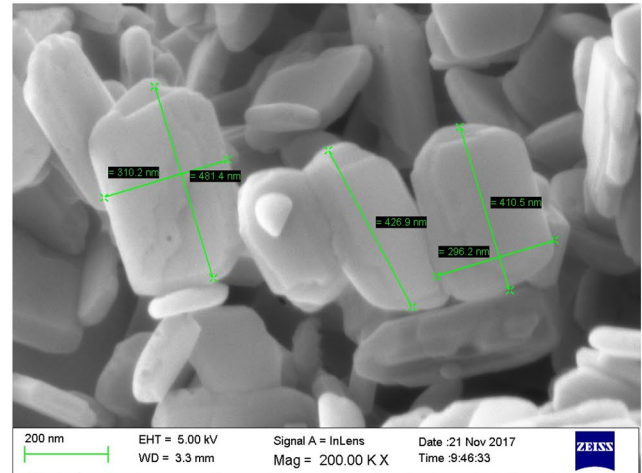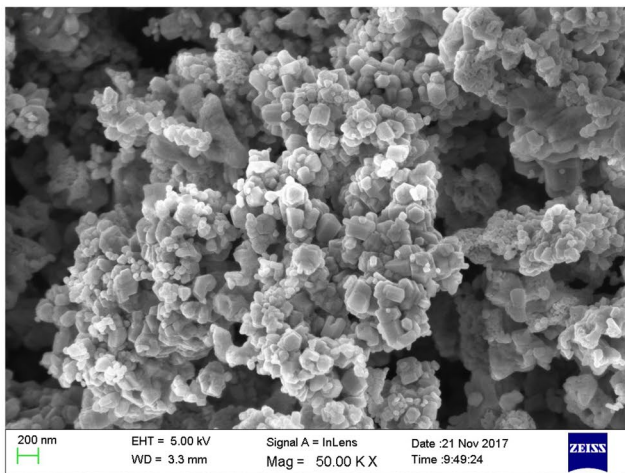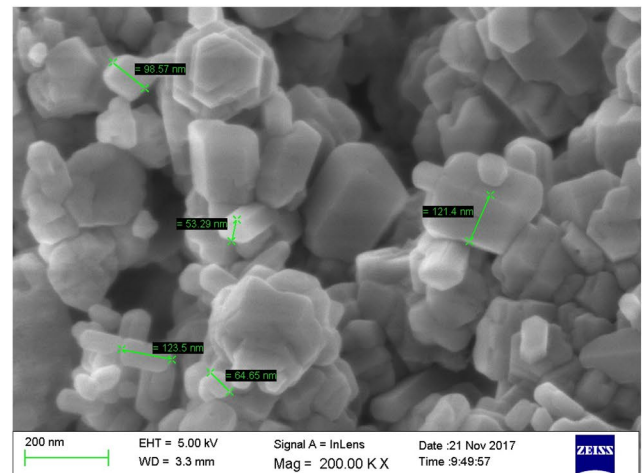
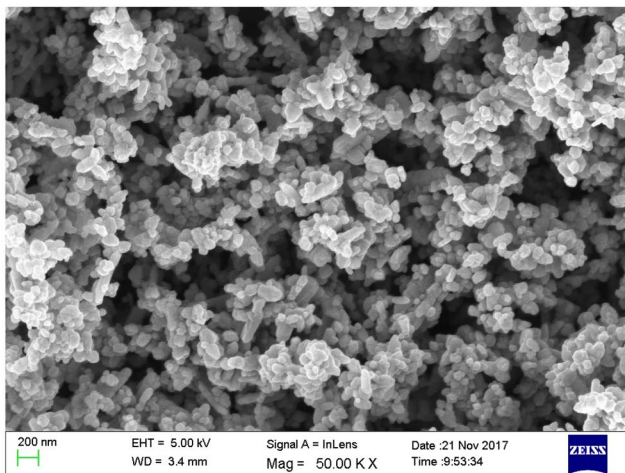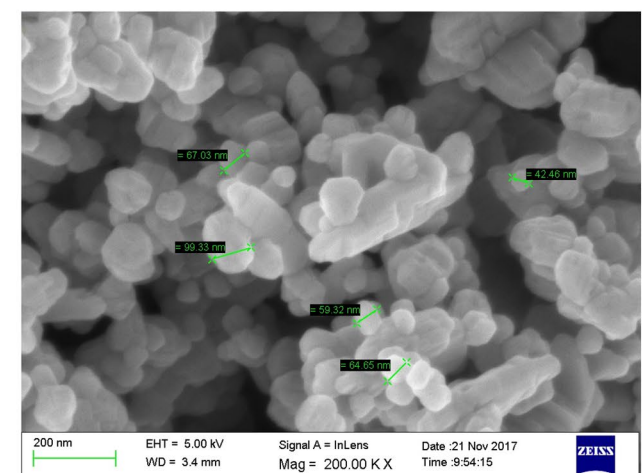**Fig. 2** **a**, **b** FESEM images of undoped ZnO. **c**, **d** FESEM images of CZO (2 wt%). **e**, **f** FESEM images of CZO (4 wt%). **g**, **h** FESEM images of CZO (6 wt%). **i** TEM image of CZO (6 wt%)
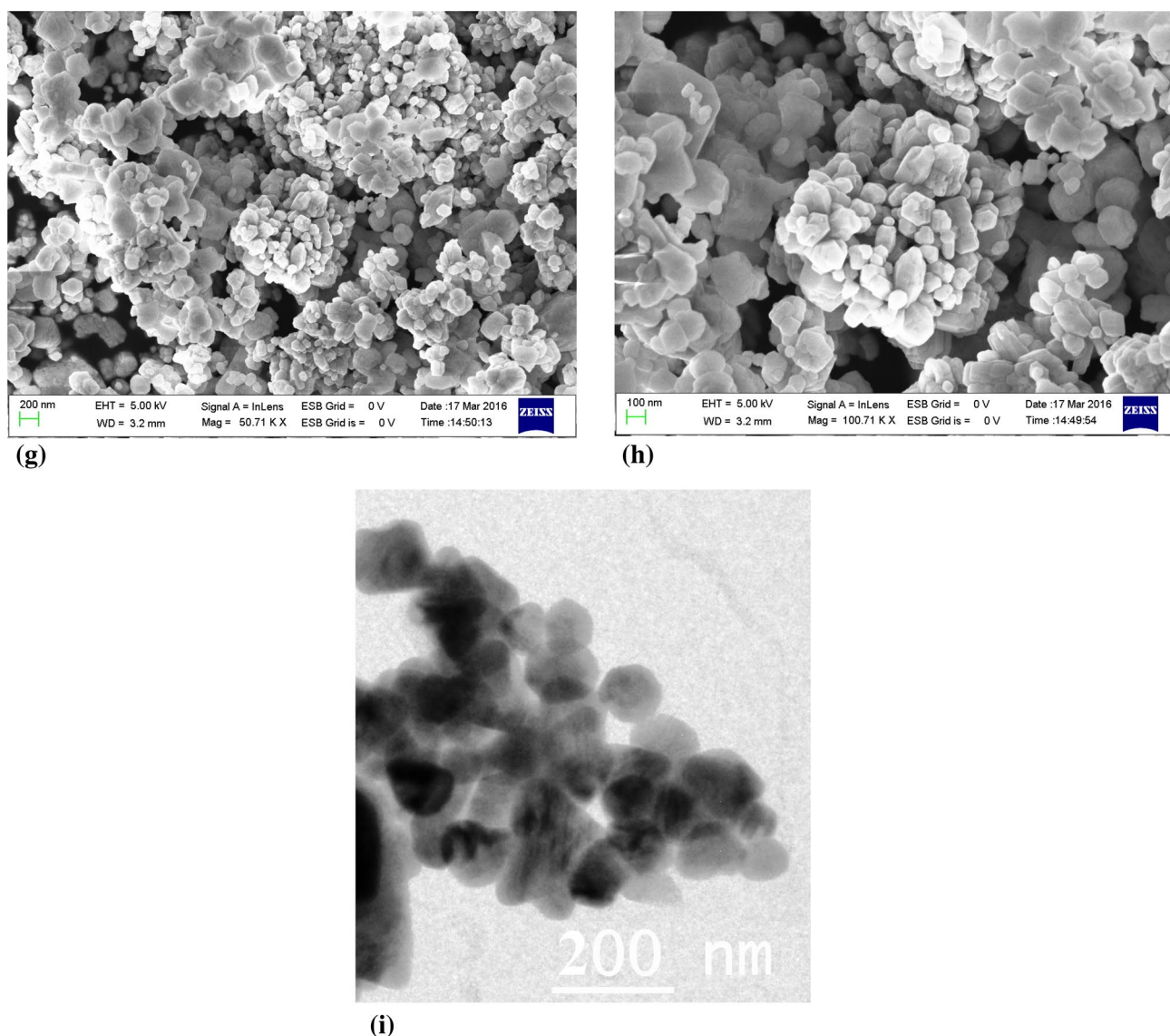
(g)

(h)

(i)

Fig. 2 (continued)

depended on its two polar planes like positive Zn terminated (0001) plane and negative O terminated (000$\bar{1}$) plane. At strong basic condition, excess amount of OH^- ions were present in the solution than Zn^{2+} ions. This OH^- ion easily adsorbed onto positive polar facets of ZnO and inhibits the crystal growth along (0001) direction. It resulted in plate-like morphology of ZnO nanostructures [33]. For the CZO material, at low concentration of Cd (2 wt%), plate-like morphology of undoped ZnO changes to tiny rod-like morphology. FESEM images showed agglomerated tiny nanorods with a length of rods was in the range of 100–120 nm as shown in Fig. 2c, d. When the concentration of Cd increased to 4 wt%, the mixture of dominant nanorods decorated with nanoparticles was observed. The diameter of nanoparticles is in the range of 40–60 nm (Fig. 2e, f). Further, the

concentration of Cd dopant was increased to 6 wt%, a compact and irregular particle with relatively uneven sizes were observed as shown in Fig. 2g, h. Thus it clearly observed that incorporation of Cd atoms into the ZnO lattice influenced the size and morphology of synthesized ZnO sample. The representative TEM image of CZO (6 wt%) in Fig. 2i revealed that the irregular shape particles with dimensions are ranging between 100 to 150 nm. The specific BET surface area for undoped ZnO and CZO (2, 4 and 6 wt%) was determined to be 14.077, 20.040, 25.330 and 19.331 m^2/g respectively. The significant increment in specific surface area of sample CZO (4 wt%) was a prominent feature for enhancement of photocatalytic activity.

3.3 Elemental analysis

The elemental composition was determined by energy dispersive spectroscopy (EDS) techniques and color mapping analysis. Figure 3a–d shows the existence of all expected elements Zn, C, O and Cd in CZO (6 wt%) sample. It confirms that presence of Cd in ZnO lattice without any other impurities.

3.4 XPS analysis

In order to investigate elemental and chemical states of undoped ZnO and CZO samples, XPS study was carried out (Fig. 4a–d). The peak of C, O, Zn and Cd in the survey spectrum of undoped ZnO and CZO (6 wt%) were detected as shown in Fig. 4a. The C1S (284.4 eV) was used for calibration. In Fig. 4b Zn 2p peaks were observed at 1016.25 eV and 1039.25 eV corresponding to $Zn2P_{3/2}$ and $Zn2P_{1/2}$ which confirms that Zn exists in divalent oxidation state [34]. The slight shift in binding energy for CZO of 23 eV, it may be due to electronic interaction between ZnO and dopant material [35]. Figure 4c represents the Gaussian fitting curve of O1S spectra of CZO (6 wt%). Two peaks centered at 529.42 eV and 531.02 eV were observed. The weak peak at 531.02 eV attributed to oxygen deficiency in Cd-doped ZnO and major peak at 529.42 eV related to lattice oxygen of doped ZnO [36]. Figure 4d shows Cd 3d XPS spectra of Cd-doped ZnO. The peak at a binding energy of 400.29 eV and 406.99 eV can be attributed to $Cd3d_{5/2}$ and $Cd3d_{3/2}$ respectively.

3.5 Optical properties

The UV–visible spectra of undoped ZnO and CZO (2, 4 and 6 wt%) were shown in Fig. 5. The absorption edge value of undoped ZnO and CZO (2, 4 and 6 wt%) were 373, 400, 400 and 413 nm respectively. The absorption edge of CZO was red-shifted as compared to undoped ZnO. The redshift in absorption edge indicated that the decrease in bandgap value with increase in doping concentration. The change in the value of E_g depends on various factors such as lattice strain, grain size, carrier concentration, etc. The reduction in bandgap may be attributed to the formation of energy levels within the conduction band and valence band.

3.6 Photoluminescent study

Photoluminescence spectroscopy is a technique to study structural defects in the semiconductor. The most probable defect observed to be oxygen vacancy (V_0), zinc vacancy (V_{zn}), oxygen interstitials (O_i) and zinc interstitials (Zn_i) [2, 37, 38]. The room temperature photoluminescent spectra of undoped ZnO and CZO were measured at an excitation wavelength of 325 nm as shown in Fig. 6. The weak band at 355 nm was a near band edge (NBE) emission and attributed to recombination of photogenerated free electron and hole

Fig. 3 **a–d** EDS pattern of CZO (6 wt%)
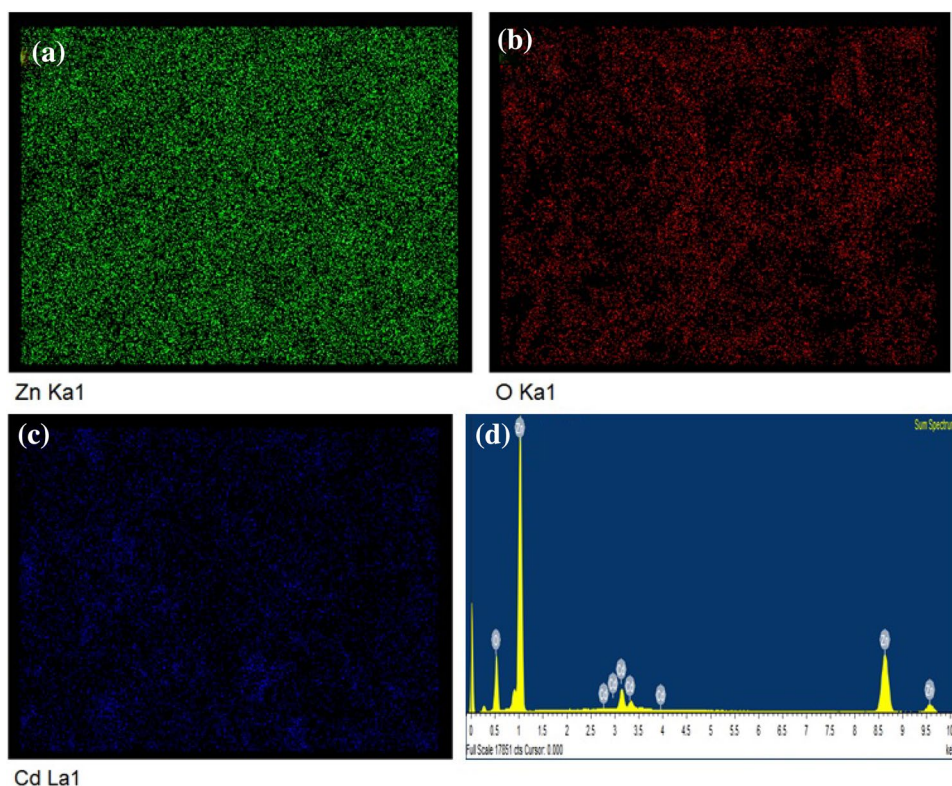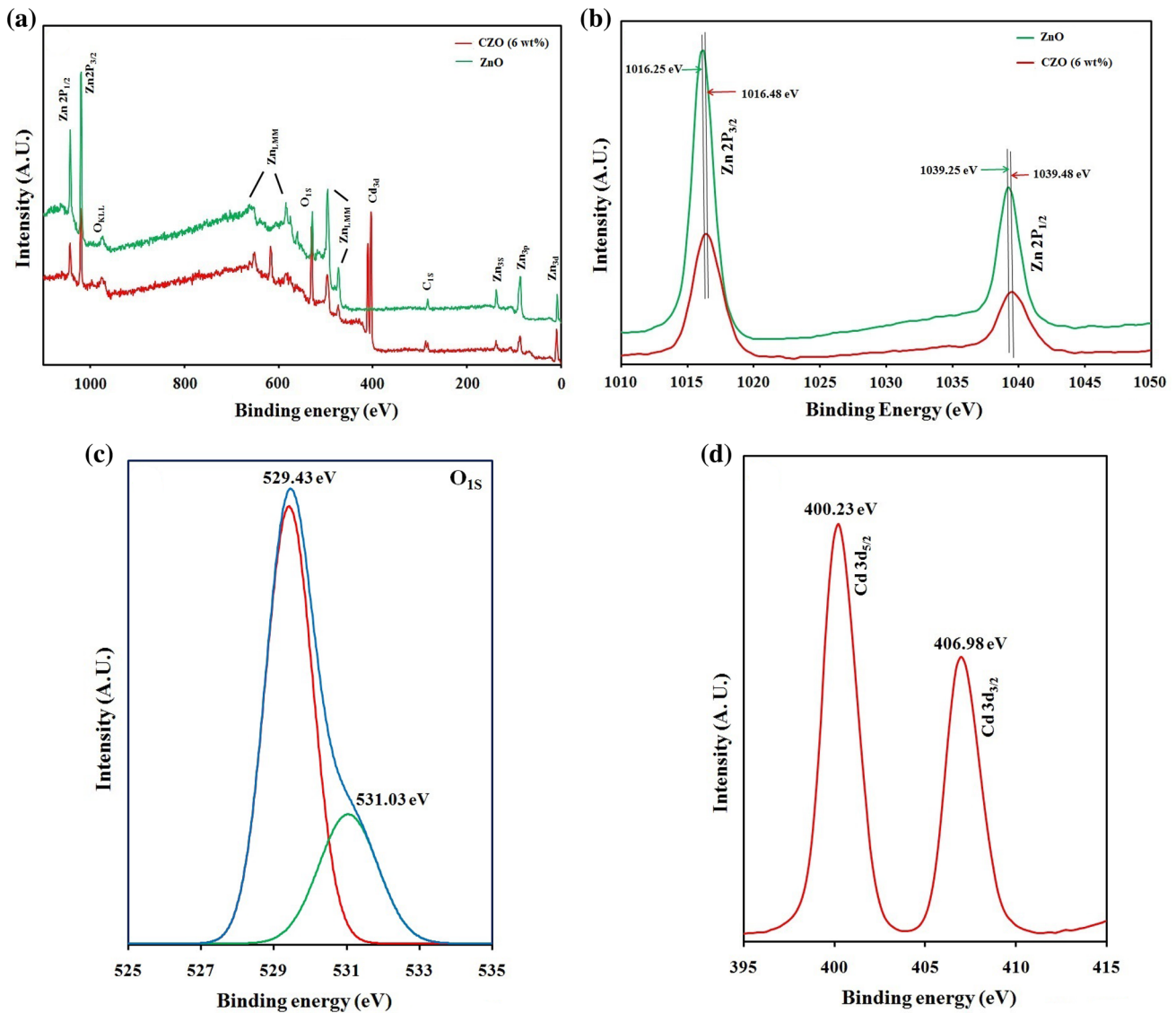
Fig. 4 **a** XPS survey spectra of undoped ZnO and CZO (6 wt%). **b** Zn2P chemical state spectrum of undoped ZnO and CZO (6 wt%). **c** O1S chemical state spectrum of CZO (6 wt%). **d** Cd3d chemical state spectrum of CZO (6 wt%)

pair [2]. The weak NBE emission indicates that dominated defect-related emission. The Cd^{2+} dopant may act as an electron acceptor for ZnO and prohibited recombination of photoexcited electron and hole pair. The reduction in electron/hole recombination rate indicates the decrease in NBE emission of CZO. The emission peak centered at 405 nm (violet) assigned to transition from zinc interstitials (Zn$_i$) to the valence band. In case of violet emission, when electrons were excited up to a sub-band of the conduction band, they can first relax to the Zn$_i$ state through non-radiative transition and transmit to the valence band. Two excitation modes such as $E_g \leq E_{ex}$ and $E_{zni} \leq E_{ex} < E_g$ were effective for violet emission. Next to violet emission, peaks observed at 428 and 457 nm were defect related blue emission. The blue emission

was due to oxygen vacancies and zinc interstitials developed during the hydrothermal growth of ZnO [33]. The different sublevels were generated below the conduction band due to oxygen vacancies. These states act as a recombination center for the electron hole pair [39]. Zeng et al. [40] reported that blue emission can be ascribe to the transition from extended Zn$_i$ state to the valence band. These extended states can be formed due to defect ionization reactions such as $Z_i^X \Leftrightarrow Zn_i^{\cdot} + e'$ and $Zn_i^{\cdot} \Leftrightarrow Zn_i^{\cdot\cdot} + e'$ and can be resulted in defect localization coupled with a disordered lattice. Hence in case of blue emission, first electron transitions was to the conduction band or Zni state, then relax to extended Zni state and eventually transition to the valence band. Three excitation modes were possible for effective blue emission
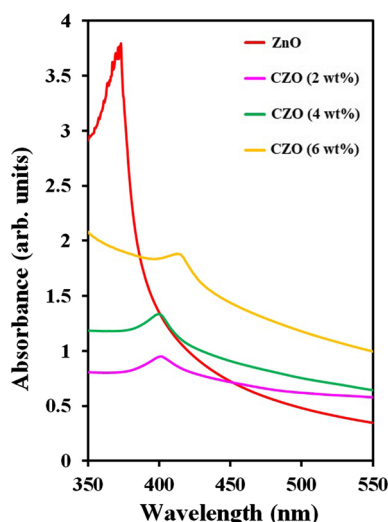
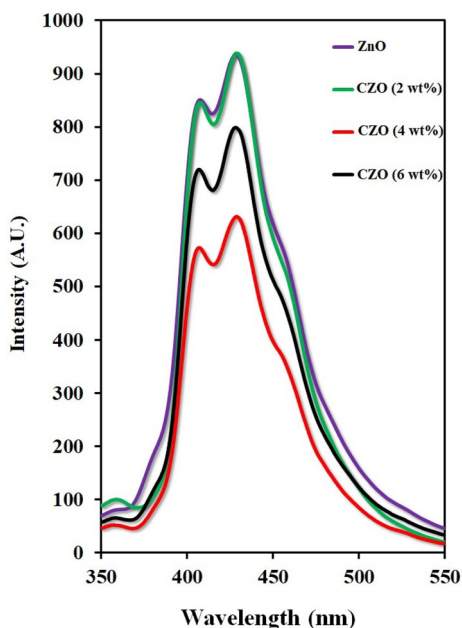**Fig. 5** UV–visible spectra of undoped ZnO and CZO (2, 4 & 6 wt%)

Fig. 6 Photoluminescence spectra of undoped ZnO and CZO (2, 4 & 6 wt%)

such as $E_g \leq E_{ex}$, $E_{Zni} \leq E_{ex} < E_g$ and $E_{ex-Zni} \leq E_{ex} < E_{Zni}$. The intensity of defect related emission was suppressed with cadmium doping indicates that the crystallinity of CZO was improved.

3.7 Photocatalytic activity

The photocatalytic study of MB dye with ZnO and CZO under sunlight irradiation has been studied. The

characteristics absorption peak of MB dye was observed at 664 nm and use to monitor the photocatalytic performance of ZnO and CZO photocatalyst. Figure 7a shows time-dependent UV–visible absorption spectra of MB dye solution in presence of undoped ZnO. It was found that the MB dye was completely degraded in 30 min for a CZO (2, 4 and 6 wt%) samples under sunlight irradiation. The CZO exhibits higher photocatalytic activity than undoped ZnO. The plot of (C_t/C_o) versus irradiation time was shown in Fig. 7b. The degradation efficiency of MB dye was 69%, 74%, 84% and 71% for undoped ZnO and CZO at 2, 4 and 6 wt% respectively. The maximum degradation efficiency was observed for CZO (4 wt%) and a further increase in doping concentration the degradation efficiency was decreased. At lower doping concentration, Cd^{2+} ion traps the photoinduced electron and reduce the recombination rate of electron and hole pair. The higher concentration of dopant acts as a recombination center for electron and hole pair due to lower defects and hence photocatalytic activity decreases [41]. As the concentration of dopant was increased, the surface barriers become higher. This leads to space charge becomes narrower and facilitate the efficient separation of electron and hole pair by internal electric field [42]. However, when the dopant concentration was beyond optimum concentration, the space charge layer becomes very narrow. The penetration depth of light into ZnO was higher than the width of the space charge layer. It leads to recombination of electron and hole pairs becomes easier [39].

The MB photodegradation was studied by using Langmuir–Hinshelwood kinetics model as follows.

$$\ln(C_o/C_t) = kt$$

where C_o is the initial concentration, C_t is the concentration at time t and k is the rate constant. The plot of $\ln(C_0/C_t)$ versus irradiation time was shown Fig. 7c. From the linear fit of the plot, rate constant was found to be 0.0293 min^{-1}, 0.0445 min^{-1}, 0.0619 min^{-1} and 0.0401 min^{-1} for undoped ZnO and CZO (2, 4 and 6 wt%) respectively. These results revealed that the photocatalytic activity was significantly improved in the presence of Cd dopant.

In order to understand the photocatalytic mechanism, active species such as holes h^+, superoxide radical $^{\cdot}O_2^-$ and hydroxyl radical $^{\cdot}OH$ were detected experimentally [15, 16, 43]. Isopropanol (IPA), benzoquinone (BQ) and edetate disodium (EDTA-2Na) were used as scavengers for $^{\cdot}OH$, $^{\cdot}O_2^-$ and h^+ respectively. Figure 7d shows the effect of scavengers IPA, BQ and EDTA-2Na on photodegradation of MB dye for CZO (4wt%) catalyst. From Fig. 7d it was clearly observed that without the addition of scavengers, MB dye showed maximum photodegradation efficiency. However, with the addition of scavengers, degradation was significantly inhibited. As IPA was added, photocatalytic degradation was decreased
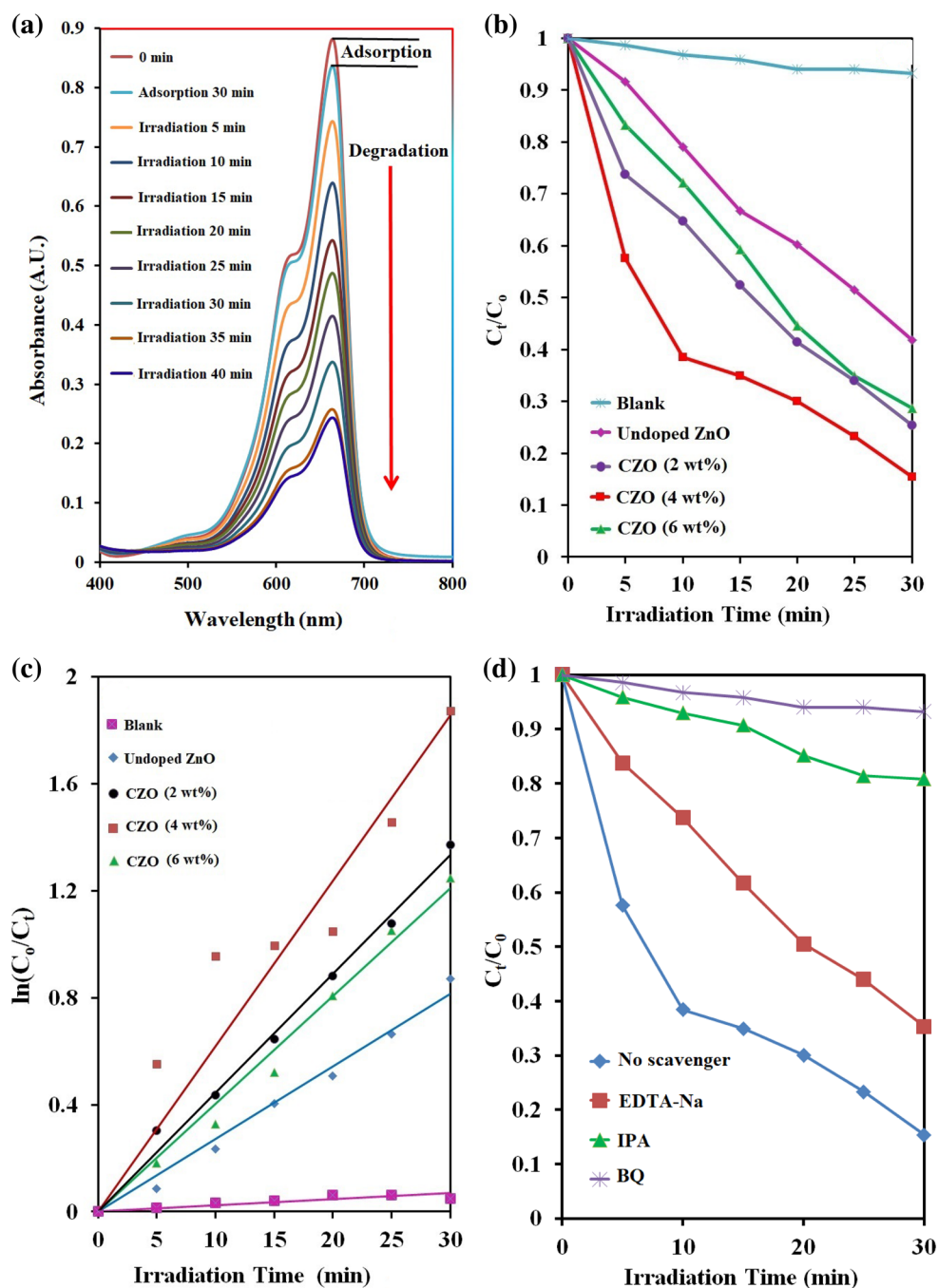
Fig. 7 a Time-dependent UV-visible absorption spectra of MB dye solution in presence of undoped ZnO. **b** Plot of C_t/C_o vs irradiation time (min) for undoped ZnO and CZO (2, 4 & 6 wt%) and without catalyst. **c** Plot of $\ln(C_o/C_t)$ vs irradiation time (min) for undoped ZnO and CZO (2, 4 & 6 wt%) and without catalyst. **d** Influence of different scavengers on the photocatalytic activity of CZO (4 wt%) sample

considerably, which confirmed that $\cdot$OH radical should be an active species during the photodegradation process. However when BQ was introduced, the photocatalytic performance was significantly restrained, indicates that $\cdot O_2^-$ active species plays a crucial role during the photodegradation process. In the case of EDTA-2Na, MB dye

was not significantly degraded and it reveals that h^+ was not acted as a main active species in the photocatalytic degradation process. As an overall effect, both superoxide radical $\cdot O_2^-$ and hydroxyl radical $\cdot$OH were the main active species and play a very crucial role in photocatalytic degradation.
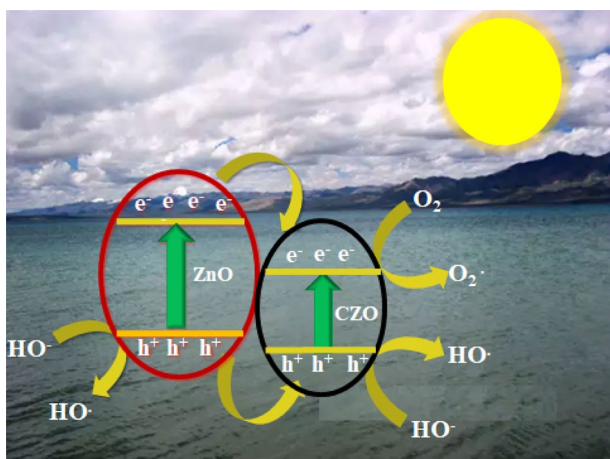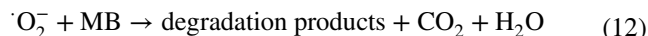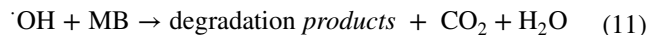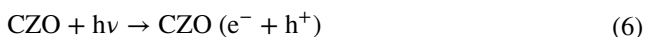
Fig. 8 Schematic representation of photocatalytic activity of CZO catalyst for the degradation of MB dye

3.8 Photocatalytic mechanism

The schematic representation of photocatalytic degradation of MB dye with CZO photocatalyst under sunlight irradiation is as shown in Fig. 8.
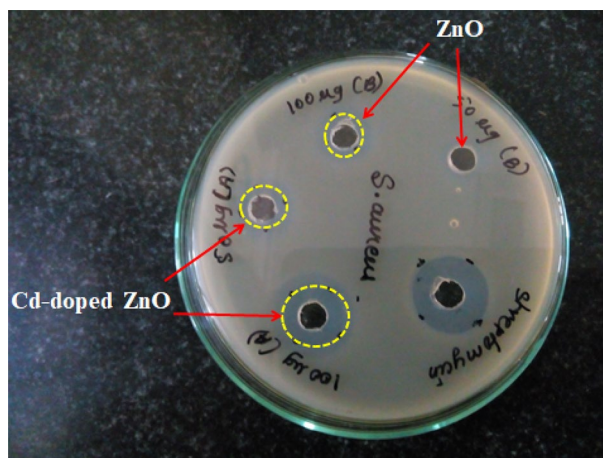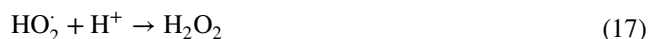
When the photocatalyst was under sunlight irradiation, the electron excited from valence band to conduction band and holes (h^+) were generated (Eq. (6)). Under sunlight illumination dopant acts as an electron scavenger and prevents electron–hole recombination. The prevention of recombination of the electron–hole pair effectively enhances the photocatalytic activity. The Cd^{2+} trap electron from conduction band of ZnO and convert into Cd^+ (Eq. (7)) [44]. Since Cd^+ ion is very unstable it reacts with an oxygen molecule and converts into Cd^{2+} with superoxide radical ($^.O_2^-$) (Eq. (8)). Zhang et al. [45] reported that cadmium has +2 oxidation state with a stable and complete electronic configuration of $4d^{10}$. As Cd^{2+} trap the electron its stable electronic configuration is distributed. Hence trap electron eventually transferred to an oxygen molecule and form superoxide radicals. However, when Cd^{2+} acts as a hole trap, its electronic configuration is again distributed. Thus trap hole transferred to surface hydroxyl anion and form hydroxyl radical. The photoinduced hole generated in the valence band of ZnO reacts with water molecule or surface hydroxyl group to generate the highly reactive hydroxyl radicals ($^.OH$) (Eq. (9, 10)). The highly reactive hydroxyl radicals ($^.OH$) and superoxide radical ($^.O_2^-$) are responsible for the degradation of MB dye (Eq. (11, 12)) [46, 47].

$$CZO + h\nu \rightarrow CZO\ (e^- + h^+) \tag{6}$$

$$Cd^{2+} + e^- \rightarrow Cd^+ (\text{electron trap}) \tag{7}$$

$$Cd^+ + O_2 \rightarrow Cd^{2+} + \cdot O_2^- (\text{electron release}) \tag{8}$$

$$H^+ + H_2O \rightarrow {}^.OH + H^+ \tag{9}$$

$$H^+ + OH^- \rightarrow {}^.OH \tag{10}$$

$$^.OH + MB \rightarrow \text{degradation } products\ +\ CO_2 + H_2O \tag{11}$$

$$^.O_2^- + MB \rightarrow \text{degradation products} + CO_2 + H_2O \tag{12}$$

3.9 Antibacterial activity

The disc diffusion method was used to study the antibacterial activity of ZnO and CZO (4 wt%) on the *Staphylococcus aureus*. It was found that the antibacterial activity of CZO shows higher inhibition efficiencies than undoped ZnO. The CZO exhibited the maximum zone inhibition of 15 mm while undoped ZnO shows zone inhibition of 10 mm. The antibacterial study of ZnO and CZO against *S. aureus* shown in Fig. 9.

The antibacterial activity of ZnO samples effectively depends on the production of reactive oxygen species (ROS) [48]. ROS usually contains free radicals such as superoxide anion radical ($^.O_2^-$), hydroxide radical ($^.OH$) and hydrogen peroxide (H_2O_2). The generation of ROS solely depends on the large surface area, oxygen vacancies and diffusion ability of reactant molecule [49]. ROS group were responsible to damage DNA, cellular protein and it leads to cell death [50]. The mechanism of generation of ROS under the illumination of light is given below,

$$ZnO + h\nu \rightarrow e^- + h^+ \tag{13}$$

$$h^+ + H_2O \rightarrow OH + H^+ \tag{14}$$

$$e^- + O_2 \rightarrow {}^. O_2^- \tag{15}$$

$$O_2^- + H^+ \rightarrow HO_2. \tag{16}$$

$$HO_2^. + H^+ \rightarrow H_2O_2 \tag{17}$$

Fig. 9 Antibacterial activity of undoped ZnO and CZO (4 wt%) against *Staphylococcus aureus*

The generated hydrogen peroxide (H_2O_2) from Eq. (17) can penetrate the cell membrane and it results in the death of bacteria [51].

Another reason for antibacterial activity was the cell membrane with a negative charge mutually attracted to the Zn^{2+} with a positive charge and hence the Zn^{2+} penetrates the cell membrane. The direct interaction between Zn^{2+} and cell membrane causes the disruption of the cell membrane of bacteria and it leads to the death of bacteria.

4 Conclusion

Undoped ZnO and CZO (2, 4, 6 wt%) nanostructures were synthesized by using the simple one-step hydrothermal method. FESEM analysis confirmed that with the introduction of Cd into ZnO, transformation of plate-like morphology of undoped ZnO into small nanorods and aggregated irregularly shaped nanoparticles. Further XPS study shows that the presence of cadmium ion into ZnO lattice and it confirms the incorporation of Cd into host lattice. The photocatalytic study suggests that the incorporation of Cd into ZnO significantly enhanced the degradation efficiency of organic dye under sunlight irradiation. CZO (4 wt%) showed maximum photodegradation efficiency of 84%. In addition, CZO (4 wt%) possess superior antibacterial activity against *S. aureus* compared to undoped ZnO. The overall study showed the hydrothermally synthesized ZnO and CZO nanostructures have potential applications in a wide area ranging from wastewater treatment to antimicrobials.

References

1. R. Dhabbe, A. Kadam, P. Kokare, M. Kokate, P. Waghmare, K. Garadkar, J. Mater. Sci.: Mater. Electron. **26**, 554 (2014)
2. K. Ghoderao, S. Jamble, R. Kale, Mater. Res. Exp. **4**, 105009 (2017)
3. Y. Su, J. Li, Z. Luo, B. Lu, P. Li, RSC Adv. **6**, 7403 (2016)
4. P. Korake, R. Dhabbe, A. Kadam, Y. Gaikwad, K. Garadkar, J. Photochem. Photobiol., B **130**, 11 (2014)
5. A. Kadam, R. Dhabbe, A. Gophane, T. Sathe, K. Garadkar, J. Photochem. Photobiol., B **154**, 24 (2016)
6. A. Ibrahim, R. Kumar, A. Umar, S. Kim, A. Bumajdad, Z. Ansarif, S. Baskoutas, Electrochim. Acta **222**, 463 (2016)
7. A. Djurisic, X. Chen, Y. Leung, A. Ng, J. Mater. Chem. **22**, 6526 (2012)
8. Z. Zang, A. Nakamura, J. Temmyo, Opt. Express **21**, 11448 (2012)
9. Y. Wu, J. Yun, L. Wang, X. Yan, Cryst. Res. Technol. **48**, 145 (2013)
10. X. Yu, F. Dong, B. Dong, L. Liu, Y. Wu, Adv. Mater. Lett. **8**, 393 (2017)
11. Y. Zhai, J. Li, X. Fang, X. Chen, F. Fang, X. Chu, Z. Wei, X. Wang, Mater. Sci. Semicond. Process. **26**, 225 (2014)
12. Y. Wang, P. Thomas, P. Brien, J. Phys. Chem. B **110**, 21412 (2006)
13. S. Zhou, X. Meng, X. Zhang, X. Fan, K. Zou, S. Wu, S. Lee, Micron **36**, 55 (2005)
14. F. Yakuphanoglu, S. Ilican, M. Caglar, Y. Caglar, Superlattices Microstruct. **47**, 732 (2010)
15. X. Yu, Y. Wu, B. Dong, Z. Dong, X. Yang, J. Photochem. Photobiol. A **356**, 681 (2018)
16. B. Dong, X. Yu, Z. Dong, X. Yang, Y. Wu, J. Sol–Gel. Sci. Technol. **82**, 167 (2017)
17. L. Wang, Y. Wun, F. Chen, X. Yang, Prog. Nat. Sci-Mater. **24**, 6 (2014)
18. N. Thirugnanam, H. Song, Y. Wu, Chin. J. Catal. **38**, 2150 (2017)
19. S. Hosseinpour-Mashkani, A. Sobhani-Nasab, J. Mater. Sci.: Mater. Electron. **28**, 16459 (2017)
20. A. Sobhani-Nasab, S. Pourmasoud, F. Ahmadi, M. Wysokowski, T. Jesionowski, H. Ehrlich, M. Rahimi-Nasrabadi, Mat. Lett. **238**, 159 (2019)
21. F. Sedighi, M. Esmaeili-Zare, A. Sobhani-Nasab, M. Behpour, J. Mater. Sci.: Mater. Electron. **29**, 13737 (2018)
22. H. Kooshki, A. Sobhani-Nasab, M. Eghbali-Arani, F. Ahmadi, V. Ameri, M. Rahimi-Nasrabadi, Sep. Purif. Technol. **211**, 873 (2019)
23. M. Eghbali-Arani, A. Sobhani-Nasab, M. Rahimi-Nasrabadi, F. Ahmadi, S. Pourmasoud, Ultrason. Sonochem. **43**, 120 (2018)
24. M. Eghbali-Arani, A. Sobhani-Nasab, M. Rahimi-Nasrabad, S. Pourmasoud, J. Electron. Mater. **47**, 3757 (2018)
25. S. Khayat, M. Abaker, A. Umar, M. Alkattan, N. Alharbi, S. Basoutas, J. Nanosci. Nanotechnol. **12**, 8453 (2012)
26. A. Phuruangrat, S. Mad-ahin, O. Yayapao, S. Thongtem, T. Thongtem, Res. Chem. Intermed. **41**, 9757 (2015)
27. A. Kaushal, D. Pathak, R. Bedi, D. Kaur, Thin Solid Films **518**, 1394 (2009)
28. B. Khoddadi, M. Bordbar, A. Yeganeh-Faal, J. Sol–Gel. Sci. Technol. **77**, 521 (2016)
29. D. Hong, G. Cao, X. Zhang, J. Qu, Y. Deng, H. Liang, J. Tang, Electrochemica Acta. **283**, 959 (2018)
30. C. Jagtap, V. Kadam, T. Ghogare, Y. Inamdar, A. Shaikh, R. Mane, A. Shaikh, J. Mater. Sci.: Mater. Electron. **27**, 12335 (2016)
31. K. Ghoderao, S. Jamble, J. Sawant, R. Kale, Mater. Res. Express **4**, 025026 (2017)
32. B. Cullity, S. Stock, *Elements of X-ray diffraction*, 3rd edn. (Prentice Hall, New Jersey, 2001)
33. K. Ghoderao, S. Jamble, R. Kale, Optik **156**, 758 (2018)
34. N. Rajamanickam, R. Mariammal, S. Rajashabala, K. Ramachandran, J. Alloys Compd. **614**, 151 (2014)
35. R. Al-Gaashania, S. Radimana, A. Dauda, N. Tabet, Y. Al-Douri, Ceram. Int. **39**, 2283 (2003)
36. S. Bai, S. Chen, Y. Zhao, T. Guo, R. Luo, D. Li, A. Chen, J. Mater. Chem. A **2**, 16697 (2014)
37. N. Fifere, A. Airinei, D. Timpu, A. Rotaru, L. Sacarescu, L. Ursu, J. Alloys Compd. **757**, 60 (2018)
38. L. Chanu, W. Singh, K. Singh, K. Devi, Results Phys. **12**, 1230 (2019)
39. R. Gupta, N. Eswar, J. Modak, G. Madras, RSC Adv. **6**, 85675 (2016)
40. H. Zeng, G. Duan, Y. Li, S. Yang, X. Xu, W. Cai, Adv. Funct. Mater. **20**, 561 (2010)
41. Y. Liang, N. Guo, L. Li, R. Li, G. Ji, S. Gan, RSC Adv. **5**, 59887 (2015)

42. S. Bai, J. Jiang, Q. Zhang, Y. Xiong, Chem. Soc. Rev. **44**, 2893 (2015)

43. A. Kadam, T. Kim, D. Shin, K. Garadkar, J. Park, J. Alloys Compd. **710**, 102 (2017)

44. D. Neena, K. Kondamareddy, H. Bin, D. Lu, P. Kumar, R. Dwivedi, V. Pelenovich, X. Zhao, W. Gao, D. Fu, Sci. Rep. **8**, 10691 (2018)

45. D. Zhang, F. Zeng, J. Mater. Sci. **47**, 2155 (2012)

46. S. Jamble, K. Ghoderao, R. Kale, J. Phys. Chem. Solids **114**, 109 (2018)

47. X. Wang, B. Zhou, Y. Zhang, L. Liu, J. Song, R. Hu, J. Qu, J. Alloys Compd. **769**, 316 (2018)

48. A. Hameed, C. Karthikeyan, V. Kumar, S. Kumaresan, G. Ravi, J. Mater. Chem. B **1**, 5950 (2003)

49. J. Becker, K. Raghupathi, J. Pierre, D. Zhao, R. Koodali, J. Phys. Chem. C **115**, 13844 (2011)

50. G. Applerot, A. Lipovsky, R. Dror, N. Perkas, Y. Nitzan, R. Lubart, A. Gedenken, Adv. Funct. Mater. **19**, 842 (2009)

51. M. Fang, J.H. Chen, X.L. Xu, P.H. Yang, H.F. Hilder, Int. Antimicrob. Agents **27**, 513 (2006)